Strain-induced performance enhancement of monolayer photodetector via patterned substrate engineering

Jianfeng Mao[1], Zehan Wu[1,2], Feng Guo[1], Jianhua Hao[1,2,*]

1 Department of Applied Physics, The Hong Kong Polytechnic University, Hung Hom, Hong Kong 999077, P. R. China

2 The Hong Kong Polytechnic University Shenzhen Research Institute, Shenzhen 518057, P. R. China

* Corresponding authors: jh.hao@polyu.edu.hk

Keywords: 2D materials, MoS_2, nanocone arrays, silicon compatible photodetector, strain engineering

Abstract: Two-dimensional (2D) materials exhibit tremendously potential for applications in the next-generation photodetectors. Up to date, approaches aiming at enhancing the device's performance are limited, relying mostly on complex hybrid systems such as heterostructures and sensitization. Here, we propose a new strategy by constructing patterned nanostructures

compatible with the conventional silicon substrate. Taking an example of CVD-grown monolayer MoS_2 on the periodical nanocone arrays, we demonstrate a high-performance MoS_2 photodetector *via* manipulating strain distribution engineered by the substrate at nanoscale. Compared to the pristine MoS_2 counterpart, the strained MoS_2 photodetector exhibits much enhanced performance, including a high signal-to-noise ratio over 10^5 and large responsivity of 3.2×10^4 A W^{-1}. The physical mechanism responsible for the enhancement is discussed by combining KPFM with theoretical simulation. The enhanced performances can be attributed to the improved light absorption, the fast separation of photo-excited carriers, and the suppression of dark currents induced by the designed periodical nanocone arrays. This work depicts an alternative method to achieve high-performance optoelectronic devices based on 2D materials integrated with semiconductor circuits.

1. INTRODUCTION

Two-dimensional (2D) materials have been attracting substantial attention in scientific and engineering research.[1-3] Among them, molybdenum disulfide (MoS_2) stands out and has been regarded as a promising candidate for the next-generation electronic and optoelectronic devices due to its excellent physical properties, such as intrinsic bandgap (1.8 eV), good stability in the atmospheric environment, outstanding strain-sensitive properties, magnetoresistance, and mechanical flexibility.[4-7] Despite these advantages, MoS_2-based photodetector has been limited by its low light absorption and short carrier lifetime, hindering the effective accumulation of photogenerated carriers and thus curtailing the further breakthrough of the device's performances.[8-10] Many methods have been developed to address these problems. For example, a

photodetector with channel length in several nanometers was prepared to decrease carrier recombination and carrier transit time, achieving ultrahigh responsivity and detectivity, with fast decay dynamics.[11] MoS_2-based heterostructures, with built-in electric filed at the hetero-interface, were designed to help separate photo-generated electron-hole (e-h) pairs, thus, enhancing photoconductive gain.[12] However, short-channel effects may induce large leakage currents, and assembling vdWHs is laborious.

Recently, integration of strain engineering in 2D electronic and optoelectronic devices has been widely reported, which can boost the pristine material properties, enhance device performances and achieve novel features.[7, 13, 14] For example, the strain-engineered MoS_2 multilayers showed significant flexo-photovoltaic effects.[15] Compressive strain was induced into bilayer MoS_2 *via in situ* epitaxial growth of 2D materials on patterned substrates directly, which can improve the sensitivity of MoS_2-based photodetectors because of the light scattering effect.[16] However, previous studies have shown that it is difficult to guarantee the success of preparation high-quality MoS_2 on the rough substrate *via* the CVD method, due to the large difference in nucleation density and growth rate of MoS_2 on the substrate with hill and valley structures.[17-19] In addition, the strain introduced in 2D materials *via* the CVD process is small and sometimes vanished after the cooling period.[16, 17] Given this, the transfer of high-quality MoS_2 to patterned substrates should be considered. Li *et al*. realized capillary-pressure induced strain in 2D materials *via* soaking of MoS_2 in an ethylene glycol (EG) solution during the PMMA transfer period.[18, 19] Although this manner might be effective to remove air bubbles between the interface of the uneven substrate and 2D materials, EG solution tends to be left in the interface due to the high boiling point and viscosity, which can significantly reduce device's performances. Furthermore, tearing of transferred 2D materials cannot be avoided in this manner. It was

reported that ethylene-vinyl acetate (EVA) can be an attractive candidate as a supporting layer for the transfer of 2D materials onto substrates with patterned features, due to its lower elastic modulus, high elongation capability, and good solubility.[20, 21] Therefore, it is necessary to study the performances of the MoS_2 photodetector based on EVA-transfer method and reveal the role of patterned substrate in improving the performances of the device.

In this study, high-quality MoS_2 monolayer was grown on a SiO_2 (300 nm)/Si substrate *via* the CVD method and transferred to flat SiO_2/Si substrate with a 10 nm TiO_2 layer and patterned nanocone substrate *via* EVA. The Raman and photoluminescence (PL) analysis were used to investigate the tensile strain in MoS_2 monolayer induced by the nanocone patterned substrate. A strained MoS_2 photodetector was fabricated and its corresponding performances, including photocurrent, responsivity, and detection capability have been characterized. Based on the Kelvin probe force microscopy (KPFM) and finite-difference time domain (FDTD) simulation results, the periodical nanocone nanostructures can help enhance light absorption and effectively promote separation of photo-generated carriers in MoS_2 and drive them from the apex to the bottom of the nanocone, resulting in significant enhancement in photoresponse of the devices. In addition, the back-to-back built-in electric field induced by nanocone can significantly lower dark currents in the strained MoS_2 photodetector. Therefore, MoS_2 photodetectors based on strain-engineering by patterned nanocone substrate exhibit high responsivity and fast response while maintaining ultrahigh photodetectivity. We offer a valuable opportunity for the design of other 2D material-based photodetectors with high performances, which can be integrated on any desired substrate and is fully compatible with present Si complementary metal oxide semiconductor (CMOS) technology for scalable applications.

2. RESULTS AND DISCUSSION

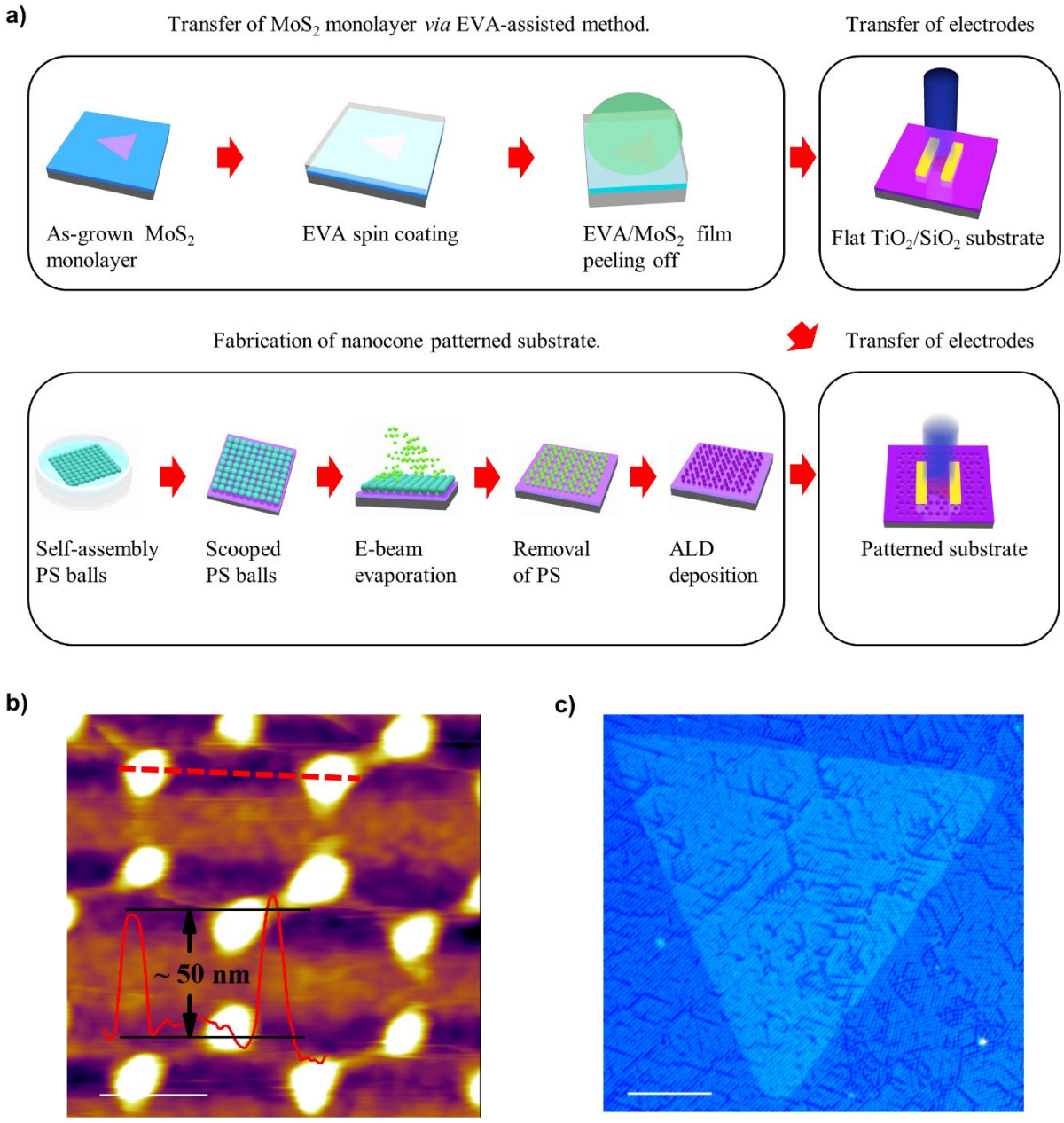

Figure 1. Fabrication process of MoS_2 photodetectors and morphology of transferred MoS_2 monolayer on the patterned nanocone substrate. (a) Schematic illustration of different steps for preparation of varied photodetector devices. (b) AFM topography of the MoS_2 monolayer on the patterned substrate. The scale bar is 0.4 μm. The inset image shows the height profile of

nanocones along the red dotted line. (c) Optical microscope image of 2D MoS_2 strained crystal. The scale bar is 10 μm.

The detailed construction procedures of our strained and unstrained MoS_2 devices are schematically illustrated in Figure 1a. In brief, the nanocone patterned substrate was fabricated by self-assembling monolayer polystyrene (PS) balls on the SiO_2 surface using the Langmuir Blodgett method. After deposition of Ti layer on the whole PS surface, hexagonal patterned substrate was achieved *via* removing PS balls with sonication method. The final product was then obtained by depositing a thin TiO_2 layer with 10 nm on the surface of the substrate. The main point in the transfer method is to pick up MoS_2/EVA film slowly from the edge with the help of DI water. (The detail is included in Methods). As is shown in Figure 1b, the hexagonal periodical array was prepared on the substrate. Once MoS_2 was transferred on the patterned substrate, it conformed tightly to the shape of nanostructures on the substrate, resulting in sharply bent MoS_2 on the nanocone. The profile line in the inset of Figure 1b shows that the height of the periodical nanocone is ~50 nm. The visible wrinkles between nanocones in AFM topography verify the presence of deformation and strain in the MoS_2 monolayer.[19, 22] The optical microscope image in Figure 1c reveals that excellent continuity of MoS_2 monolayer can be achieved on the whole patterned substrate *via* EVA-transfer method, without observable cracks or tears. However, severely broken phenomenon easily occurred in MoS_2 crystals using the conventional PMMA-transfer method (see Figure S 1).

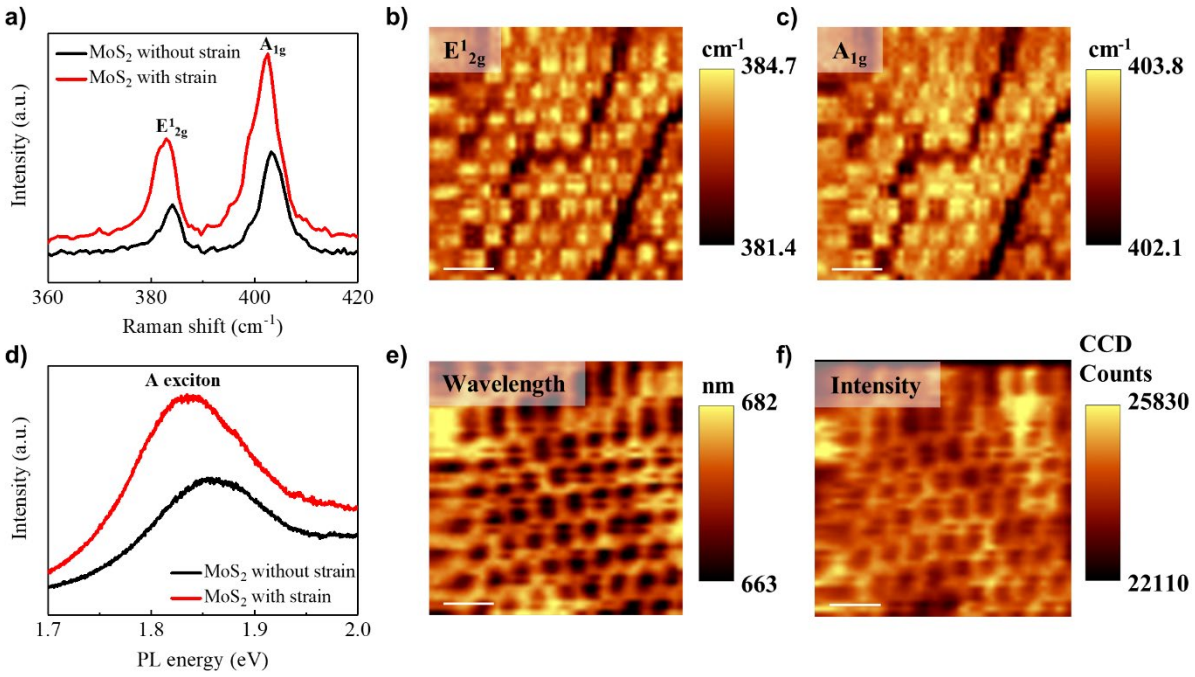

Figure 2. Raman and PL spectroscopy of the strained MoS_2 monolayer on the patterned substrate. (a) Comparison of Raman spectra for MoS_2 on top of nanocone and in flat regions among nanocones. Raman mapping images displaying (b) E^1_{2g} peak frequency and (c) A_{1g} peak frequency of strained MoS_2 on the nanocone substrate. (d) Comparison of PL spectra for MoS_2 at apex and perimeter of the nanocone. PL spectroscopic maps with (e) peak wavelength and (f) intensity for MoS_2 on the patterned substrate. Scale bars are 1 μm.

Micro-Raman spectroscopy was used to investigate the spatial strain distribution of MoS_2 monolayer on the patterned substrate. Figure 2a shows the Raman spectra of strained and unstrained MoS_2. Two dominant modes (E^1_{2g} at ~384.2 cm^{-1} and A_{1g} at ~403.1 cm^{-1}) are observed for unstrained MoS_2 in flat regions, which are characteristic peaks of MoS_2 monolayer.[23, 24] While for Raman spectra of strained MoS_2 on the nanocone top, significant

redshift behaviors are found for both E^1_{2g} and A_{1g} peaks (1.4 cm^{-1} and 0.5 cm^{-1}, respectively). According to previous studies, the Raman shift can be strongly associated with the strain introduced in the TMDCs due to the change of lattice constant.[25, 26] Normally, the red-shifted Raman spectra indicate the tensile strain in TMDC, while a blueshift represents the compressive strain. As a result, the redshift of Raman spectra found in strained MoS_2 monolayer can be attributed to a tensile strain. (Strain of 0.27% and 0.29% can be calculated from the redshifted magnitude of E^1_{2g} and A_{1g} modes respectively) [27, 28]. The Raman mappings of E^1_{2g} (Fig. 2b) and A_{1g} (Fig. 2c) peak frequencies show that varying strain is periodically distributed, following the pattern of the substrate over the entire scanned area (25 μm^2). The highest strain occurs on the apex of nanocone, while it becomes lowest in the flat regions among nanocones. Micro-PL spectroscopy was adopted to study the band gap of strained MoS_2 monolayer on the patterned substrate. Figure 2d compares PL spectra of strained and unstrained MoS_2. The PL spectrum of unstrained MoS_2 samples shows a typical peak for MoS_2 monolayer at 1.86 eV (A exciton), while a redshift of 27.7 meV is found for the PL peak of strained MoS_2.[29] This indicates that the band gap of MoS_2 monolayer can be effectively tailored *via* transferring MoS_2 on the patterned substrate. From the magnitude of the redshift in the PL peak, a tensile strain of 0.28% is inferred to be induced in MoS_2 2D samples, which agrees well with the strains obtained from Raman analysis above.[27, 28] It should be noted that the PL intensity for strained MoS_2 is much stronger than that of unstrained counterpart and the distribution of PL intensity is highly reproducible over the whole scanned area (Figure 2f). The observed PL enhancement can be explained by the multiple internal reflection and absorption model, known as Fabry−Perot interference, which is shown in Figure S 2.[30] When the incident light encounters the boundary of air/MoS_2, some is reflected from the MoS_2 surface, some is absorbed in MoS_2 and the rest is transmitted and

reaches the surface of the metal (Ti). The transmitted light at the Ti surface can be reflected and absorbed in MoS_2 again, resulting in strong interaction between MoS_2 and light. On the other hand, the patterned nanostructure on the substrate can induce a strong localized electric field on the nanocone, leading to further enhancement of PL emission, which will be discussed further in the following part. In addition, PL wavelength mapping (Fig. 2e) shows the periodical modulation of MoS_2 band gap over the whole scanned areas, nicely following the AFM topography of the transferred MoS_2.

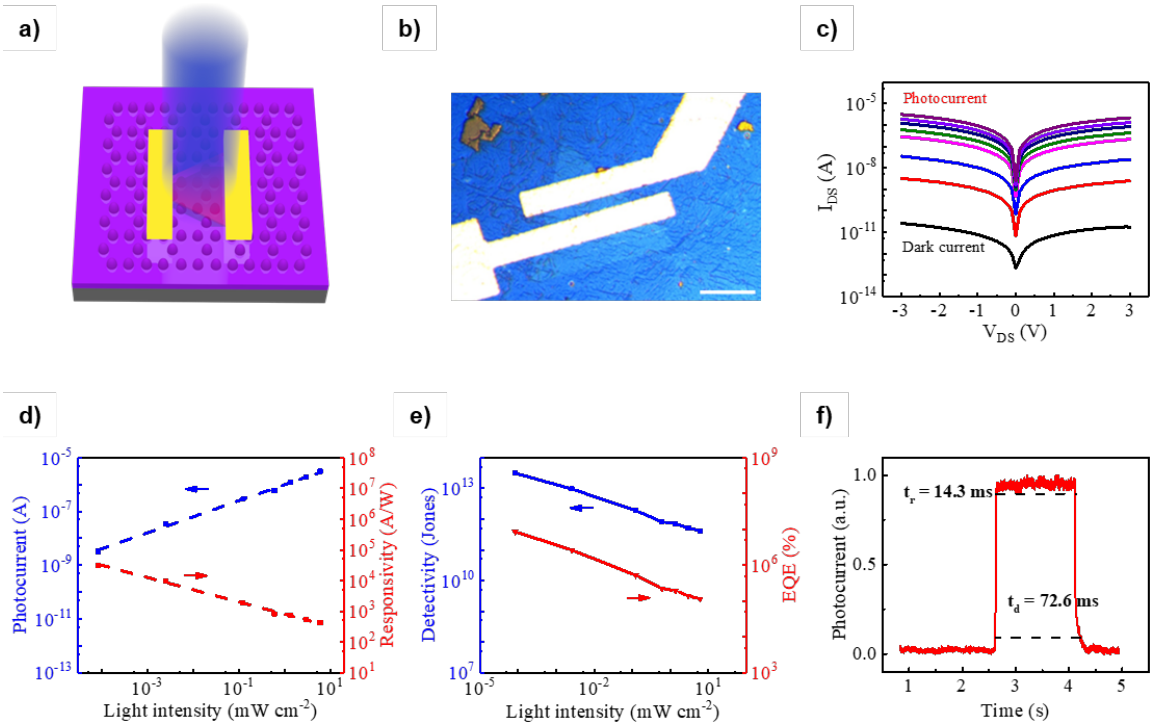

Figure 3. Performances of strained MoS_2 photodetectors. (a) Schematic illustration and (b) the optical microscopy image of strained MoS_2 photodetectors on the nanocone substrate. The scale bar is 20 μm. (c) Logarithm *I–V* characteristics of photodetectors measured in the dark and at 460 nm light illumination with the light intensities varying from 8.4×10^{-5} to 5.98 mW cm^{-2}. (d)

Photocurrent (I_{ph}) and responsivity (R), as well as (e) external quantum efficiency (EQE) and detectivity (D^*) of photodetectors under different illumination intensities at a fixed 3 V bias. (f) Temporal photocurrent response of the photodetectors.

Then, the optoelectronic detection properties of strained MoS_2 photodetectors on the patterned substrate are systematically investigated in Figure 3. The prototype device shown in Figure 3a and 3b was fabricated by transferring 50 nm Au electrodes on the intact MoS_2, where the channel length and width are ~4 μm and ~30 μm respectively. Firstly, I–V curves of strained MoS_2 photodetectors measured under the dark and varied light illumination intensities are presented in Figure 3c. The dark current is estimated to be only 1.7×10^{-11} A at a bias of 3 V. Moreover, the photocurrent shows a significant enhancement with illumination intensity and reaches up to 3.1×10^{-6} A at 5.98 mW cm^{-2}, resulting in a high signal-to-noise ratio over ~10^5. The relationship between photocurrent and driving voltage exhibits near-linear and symmetric behaviors, indicating good contacts between the MoS_2 monolayer and transferred Au electrodes. Noteworthily, the present strained MoS_2 photodetector is very sensitive to illumination even at a weak light intensity, which offers new avenues to design photodetectors with a high signal-to-noise ratio in practical applications.

The key figures of merit to quantificationally evaluate photodetectors including R, D^*, EQE, and response time are defined in detail in SI Note 1. It can be seen from Figure 3c that the photocurrent measured at 3 V exhibited a positive and linear correlation with illumination intensity, due to the increase of photogenerated carriers. This photocurrent curve can be well fitted with a simple power law, $I_P \sim P^{\theta}$, where θ determines the device photoresponse to the

illumination light. The linear-fitting line provides $\theta = 0.6$, which is smaller than 1 (for an ideal photodetector). This indicates the existence of trap states between the Fermi level and the conduction band edge in MoS_2 or at the interface of the substrate. In contrast, the responsivity shows the decline at higher illumination power and reached its maximum at 3.2×10^4 A W^{-1}. This reduction can be explained by the saturation of trap states upon the increasing illumination intensity.[31, 32] The significantly high detectivity, $D^* = 3.1 \times 10^{13}$ Jones (cm $Hz^{1/2}$ W^{-1}), is achieved at the excitation wavelength of 460 nm due to the low dark current (see Figure 3e). *EQE* shows a similar declining trend as the D^* and the corresponding maximum value is calculated to be 8.6×10^6 %. In order to investigate photo-switching properties of the prepared devices, the incident light on/off was controlled by a signal function generator as a power supply, which can produce a 50% duty cycle square waveform with fast rise and fall time to modulate the light. Then the photoresponse of the devices over a complete on/off cycle was obtained in the high temporal resolution mode under a bias of 3 V. Figure 3f shows the temporal photocurrent response of the strained MoS_2 photodetectors triggered by periodic illumination with the intensity of 5.98 mW cm^{-2}. The rise time (t_r) and drop time (t_d) of the device is estimated to be 14.3 ms and 72.6 ms, indicating a fast response speed of the device to the light intensity.

For comparison, optoelectronic performances of the pristine MoS_2 photodetector are summarized in Figure S 4, where the channel length and width are ~4 μm and ~ 36μm respectively. The dark current of the device is approximately nA level, which is almost two orders of magnitude higher than that of the strained MoS_2 photodetector. Noteworthily, the photocurrent detected at 8.4×10^{-5} mW cm^{-2} shows no difference from the dark current. Thus, photocurrents of pristine MoS_2 were measured at light intensities from 2.58×10^{-3} to 5.98 mW cm^{-2}. The higher dark current and lower photocurrent lead to poor performance in the signal-to-noise ratio (~ 10^3) for the

pristine MoS_2 photodetector. Moreover, the derived *R*, *D**, *EQE,* and photodetection dynamics values of this photodetector is estimated to be 5.2×10^2 A W^{-1}, 7.2×10^9 Jones, 1.4×10^5 %, and 26.3 s/18.9 s, respectively, which are significantly lower than those of strained MoS_2 photodetectors. We also compare our strained MoS_2 photodetector with a series of previously reported state-of-the-art MoS_2-based photodetectors and the results are summarized in Table S 1. It is evident to see from results above that the strained MoS_2 photodetector stands out from all these reported devices in comprehensive consideration of signal-to-noise ratio, *R*, *EQE*, *D**, and detection dynamics. Therefore, MoS_2 photodetectors engineered by the nanocone substrate provide a convenient and scalable method to prepare high-performance optoelectronic devices, in comparison with those previously reported approaches, such as heterostructures[33] and narrow channel length[11] that are sophisticated and high-demanding in equipment.

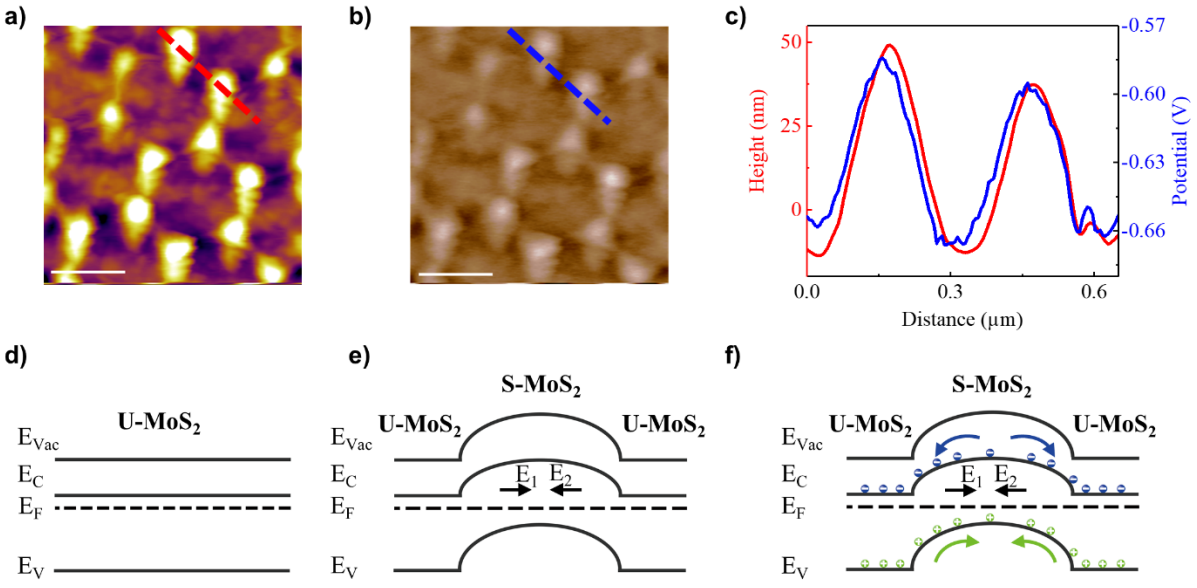

Figure 4. The mechanism analysis of strained MoS_2 photodetector. (a) AFM and (b) KPFM images of the MoS_2 monolayer on the nanocone substrate. The scale bar is 400 μm. (c) Corresponding height and surface potential profile along the dotted line. Energy band structures of (d) unstrained MoS_2 and (e) strained MoS_2. (f) Energy band structure and transport behaviors of photogenerated charges in strained MoS_2 photodetector under light illumination.

In order to explain the enhanced photoresponse properties of strained MoS_2 on nanocone substrate, KPFM measurement was carried out. In principle, KPFM can acquire localized charge transport in TMDC by collecting the information of surface potential distribution in micro regions. Similar to the hexagonal pattern as the corresponding AFM topography (Figure 4a), the surface potential for MoS_2 is illustrated in Figure 4b. The obvious enhancement (by ~ 80 mV) in surface potential is found for strained MoS_2 on the nanocone tip, compared with that of on the flat area (Figure 4c). In order to exclude the possibility that the potential difference is induced by the nanocone itself, KPFM measurement was carried out on the pure nanocone substrate (Figure S 5). The potential change induced by nanocone is only ~ 10 mV, much smaller than that for the strained MoS_2. The difference in surface potential for MoS_2 indicates that the work function of MoS_2 can be significantly enhanced *via* strain engineering of the nanocone on the substrate. Accordingly, the higher work function for MoS_2 on the nanocone forms a "barrier height" region with a back-to-back built-in electric field (E_1 and E_2) from unstrained MoS_2 to strained MoS_2 (Figure 4f). This "barrier height" can effectively suppress the electron transport in the dark, resulting in a lower dark current of the device. On the other hand, under light illumination, both strained MoS_2 and unstrained MoS_2 generate electron-hole pairs. These photoexcited carriers can be separated quickly with the formed built-in electric field, leading to the enhancement of

photoresponse dynamics and photocurrent of the device.[16] Both the effective suppression of dark current and enhanced transportation of photoexcited carriers reveal that 2D materials engineered by nanocone substrate are suitable for the application of high-performance optoelectronic devices.

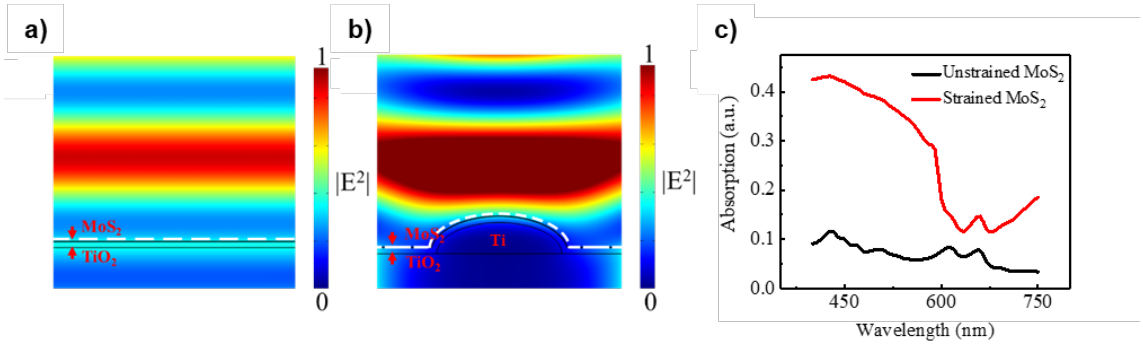

Figure 5. FDTD simulation of the electric field at the illuminated light with 460 nm. (a) The exciton-generated densities for the MoS_2 monolayer on (a) flat and (b) nanocone substrates. (c) Absorption spectra of MoS_2 monolayer on different patterned substrates.

To further understand the enhancement performances of strained MoS_2 photodetector, FDTD models were built by the COMSOL software to investigate the electric field distribution under the illumination light of 460 nm. According to simulation results in Figure 5a, the calculated spatial profiles of electric field intensity ($|E|^2$) concerning the *x*–*z* plane is periodical, indicating no relationship of incident light with the flat substrate. However, the intensity of the electric field for strained MoS_2 on the nanocone substrate is significantly enhanced (Figure 5b). The generation rate of photo excitons in MoS_2 can be described by Fermi's golden rule[34]

$$\Gamma = \frac{2\pi}{\hbar}|\vec{d}\cdot\vec{E}|^2\rho(\omega) \quad (1)$$

where $\vec{E}$ is the electric field, $\vec{d}$ is the effective exciton dipole moment and $\rho(\omega)$ is the density of electromagnetic mode. Thus, the photogenerated excitons for MoS_2 monolayer are proportional to the electric field intensity. The localized electric field in the nanocone structure indicates that excited photons tend to be concentrated in this region under the vertical illumination light. Such a phenomenon can be explained by the localized surface plasmon effect induced by the TiO_2/metal patterned nanocone structure on the substrate. This agrees well with the observed phenomenon that the PL intensity for strained MoS_2 is stronger compared with that for unstrained MoS_2. The localized photo-generated carriers are then separated quickly and driven to migrate from the top to the bottom of the nanocone due to the built-in electric field. The light absorption spectra of MoS_2 monolayer on different kinds of substrate are presented in Figure 5c. The results show that the strained MoS_2 monolayer on the nanocone substrate exhibits much higher light absorption capability, compared with the MoS_2 on the flat substrate, due to the Fabry−Perot interference and localized plasmonic effect of the periodical nanostructures on the substrate. Furthermore, the strained MoS_2 monolayer can absorb a maximum percentage of incident light at around 450 nm. Both the strong light interaction with MoS_2 and enhanced light absorption ability induced by nanocone substrate results in excellent performances of the strained MoS_2 photodetector in this work. Finally, we compare light absorption and photocurrent enhancement ratios in SI Table 2 while assuming the unstrained MoS_2 photodetector as a reference. It is worth noting that the enhancement ratio for photocurrent of strained MoS_2 photodetectors can reach 14.4 at low light intensity (2.58 μW cm^{-2}) and then gradually decays to ~4 with the illumination intensity increasing. The photocurrent in different photodetectors can be summarized as follows.

$$I_P = \frac{e\eta}{h\upsilon} M P_{ab} \tag{2}$$

where e is the elementary charge, h is Planck's constant, η is the quantum efficiency, M is the photocurrent gain, and P_{ab} and υ are the intensity and frequency of absorption light respectively. The final photocurrent can be determined by three main factors, namely, P_{ab}, M, and η. When the illumination intensity is weak, η is independent of P_{ab} and the amount of enhancement for P_{ab} can fully contribute to the generation of photocurrent. For unstrained MoS_2 photodetectors, the photocurrent gain

$$M = \frac{V\mu_n\tau_n}{L^2} \tag{3}$$

where τ_n is the exciton lifetime, μ_n is the electron mobility, V is the applied voltage and L is the channel length. τ_n and μ_n are calculated to be ~800 ps and 2.1 $cm^2 V^{-1} s^{-1}$ at room temperature respectively[35]. Thus, M is obtained to be ~0.03 for the unstrained MoS_2 photodetector. While for strained photodetectors, the drift length of excitons is 660 nm, much larger than the width of built-in electric field.[19] The recombination of excitons in the depletion region can then be neglected, resulting in M equaling 1. Considering the effective area of depletion regions formed by nanocone arrays in the strained MoS_2 photodetector, the final photocurrent enhancement ratio (14.4) matches with the multiplication of area, P_{ab}, and M enhancement ratios (16.3) under weak light intensity (see SI Note 2). However, when the input light intensity is strong, the recombination rate of photogenerated carriers will be increased, leading to a decrease in quantum efficiency (η).[36] On the other hand, the trap states on the surface of substrate tend to be saturated under strong light illumination, which indicates a lower M value with higher light intensity. Both above-mentioned reasons lead to the decay phenomenon for photocurrent ratio with the light intensity.

3. CONCLUSIONS

In summary, we have demonstrated a high-performance MoS_2 photodetector with strain engineered by the nanocone arrays on the patterned substrate. The effective EVA-transfer method ensures the continuity and tight contact of transferred MoS_2 with the nanocone arrays. Compared with the pristine MoS_2 photodetector, the pronounced performance improvement has been exhibited. The strained MoS_2 photodetector shows an excellent signal-to-noise ratio, large responsivity, high detectivity, and EQE of over 10^5, 3.2×10^4 A W^{-1}, 3.1×10^{13} Jones, and 8.6×10^6 % respectively. These performance metrics are orders of magnitude higher than those of a pristine MoS_2 photodetector. In addition, the dark current and detection dynamics of a strained MoS_2 photodetector are decreased to 1.7×10^{-11} A and 14.3 ms/72.6 ms from nA level and 26.3 s/18.9 s respectively for the pristine MoS_2 photodetector. Based on the KPFM and theoretical simulation analysis, the performance enhancement is associated with the localized built-in electric field, Fabry−Perot interference, and localized plasmonic effect induced by nanocone arrays on the patterned substrate, which can effectively suppress electron transport in dark, fast separate carriers under light illumination and enhance light absorption capability in MoS_2. More importantly, the presented substrate nanoengineering is expected to be expanded to produce other types of optoelectronic devices based on different ultrathin materials. Therefore, this high-performance MoS_2 photodetector enlightens the potential application of 2D material-based optoelectronic devices in the strategy of strain engineering by the periodical nanostructures on any desired substrate.

4. METHODS

Growth of Monolayer MoS_2. MoS_2 monolayer was grown by the CVD method on the SiO_2/Si substrate. The substrate was put upside down in a quartz tube containing a powder mixture of 10 mg MoO_3 (≥ 99.5%, Sigma-Aldrich) and 5 mg NaCl (≥ 99.5%, Sigma-Aldrich). Another

crucible full of S (powder) (≥ 99.5%, Sigma-Aldrich) was placed upstream. The temperature of S and MoO_3 was heated to 180 and 850 °C, respectively, in 30 min and were kept for 8 min for the growth of MoS_2 monolayer in the atmosphere of 50 sccm Ar. After synthesis, the system was naturally cooled down to room temperature.

EVA-Supported MoS_2 Transfer. After growth of MoS_2, EVA solution (Aldrich, vinyl acetate 40 wt %, 10 wt % dissolved in xylene) was spin coated (4000 rpm for 60 s) onto the sample, followed by baking in an oven at 80 °C for 60 min. The EVA/MoS_2 was peeled off from the grown substrate with the assistance of DI water, then fished by the target substrate. After baking at 80 ºC for 2 h, the sample was soaked in xylene for 30 min to remove the EVA film, leaving a clean and intact MoS_2 monolayer on the target substrate.

Substrate Preparation. The Ti film (~ 100 nm) was deposited via E-beam evaporation on the SiO_2 (300 nm)/Si substrate with self-assembly PS arrays. After removing PS balls, the thin TiO_2 layer (10 nm) was deposited on patterned substrates by atomic layer deposition (ALD) at 100 ºC with tetrakis (dimethylamino) titanium (TDMAT) as a source and deionized (DI) water as an oxidation agent.

Characterization. The Raman and PL investigations were carried out using a WITEC alpha 500 Confocal Raman system equipped with the 532-nm laser source. The Raman and PL spectra were collected by an Olympus 100 × objective (N.A. = 0.9) and dispersed by 1,800 (for Raman measurements) and 300 (for PL measurements) lines per mm gratings, with excitation laser power lower than 1 mW. The surface potential of MoS_2 was probed by KPM mode using the Asylum Research MFP-3D system. The morphology of the patterned substrate was further scrutinized by AFM in AC mode with a non-conductive tip (PPP-RT-NCHR, Nanoworld).

Electrical Output Measurements. The strained MoS_2 photodetectors were characterized through Keithley 4200A-SCS equipped with a probe station (Lake Shore Model CRX-6.5K) at room temperature. A 460 nm monochromatic LED was adopted as the light source for the photodetection measurements. The power of the LED was calibrated using a power meter (SANWA, LP1). For temporal photo-response measurement, LED on/off was controlled by a signal function generator as a power supply.

FDTD Solution Simulations. A finite element package (COMSOL) was used to simulate the distribution of electric fields and absorption spectra of MoS_2. Periodic boundary conditions were used for the X-axis and Y-axis, while the Z-axis uses a perfectly matched layer and the smallest mesh size in the structure was set to 0.5 nm. The electric field distribution and absorption spectra of MoS_2 monolayer on nanocone substrate were simulated.

brief description (file type, i.e., PDF)

ASSOCIATED CONTENT

AUTHOR INFORMATION

Corresponding Author

* Jianhua Hao - Department of Applied Physics, The Hong Kong Polytechnic University, Hung Hom, Hong Kong 999077, P. R. China; The Hong Kong Polytechnic University Shenzhen Research Institute, Shenzhen 518057, P. R. China;

Email: jh.hao@polyu.edu.hk

Authors

Jianfeng Mao - Department of Applied Physics, The Hong Kong Polytechnic University, Hung Hom, Hong Kong 999077, P. R. China

Zehan Wu - Department of Applied Physics, The Hong Kong Polytechnic University, Hung Hom, Hong Kong 999077, P. R. China; The Hong Kong Polytechnic University Shenzhen Research Institute, Shenzhen 518057, P. R. China

Feng Guo - Department of Applied Physics, The Hong Kong Polytechnic University, Hung Hom, Hong Kong 999077, P. R. China

Notes

The authors declare no competing financial interest.

ACKNOWLEDGMENT

This work was supported by the grants from Research Grants Council of Hong Kong (GRF No. PolyU 15301121 and SRFS 2122-5S02) and National Natural Science Foundation of China (No. 51972279).

REFERENCES

(1) Wu, Z.; Lyu, Y.; Zhang, Y.; Ding, R.; Zheng, B.; Yang, Z.; Lau, S. P.; Chen, X. H.; Hao, J. *Nat. Mater.* **2021,** 20, (9), 1203-1209.

(2) Guo, F.; Song, M.; Wong, M. C.; Ding, R.; Io, W. F.; Pang, S. Y.; Jie, W.; Hao, J. *Adv. Funct. Mater.* **2021,** 32, (6), 2108014.

(3) Yuan, S.; Pang, S.-Y.; Hao, J. *Appl. Phys. Rev.* **2020,** 7, (2), 021304.

(4) Jie, W.; Yang, Z.; Zhang, F.; Bai, G.; Leung, C. W.; Hao, J. *ACS Nano* **2017,** 11, (7), 6950-6958.

(5) Bertolazzi, S.; Brivio, J.; Kis, A. *ACS nano* **2011,** 5, (12), 9703-9709.

(6) Butler, S. Z.; Hollen, S. M.; Cao, L.; Cui, Y.; Gupta, J. A.; Gutiérrez, H. R.; Heinz, T. F.;

Hong, S. S.; Huang, J.; Ismach, A. F. *ACS nano* **2013,** 7, (4), 2898-2926.

(7) Gant, P.; Huang, P.; Pérez de Lara, D.; Guo, D.; Frisenda, R.; Castellanos-Gomez, A. *Mater. Today* **2019,** 27, 8-13.

(8) Jiao, L.; Jie, W.; Yang, Z.; Wang, Y.; Chen, Z.; Zhang, X.; Tang, W.; Wu, Z.; Hao, *J. Mater. Chem. C* **2019,** 7, (9), 2522-2529.

(9) Xiao, P.; Mao, J.; Ding, K.; Luo, W.; Hu, W.; Zhang, X.; Zhang, X.; Jie, J. *Adv. Mater.* **2018,** 30, (31), e1801729.

(10) Wang, W.; Zeng, X.; Warner, J. H.; Guo, Z.; Hu, Y.; Zeng, Y.; Lu, J.; Jin, W.; Wang, S.; Lu, J.; Zeng, Y.; Xiao, Y. *ACS Appl. Mater. Interfaces* **2020,** 12, (29), 33325-33335.

(11) Lee, I.; Kang, W. T.; Kim, J. E.; Kim, Y. R.; Won, U. Y.; Lee, Y. H.; Yu, W. *ACS Nano* **2020,** 14, (6), 7574-7580.

(12) Shin, G. H.; Park, C.; Lee, K. J.; Jin, H. J.; Choi, S.-Y. *Nano Lett.* **2020,** 20, (8), 5741-5748.

(13) Maiti, R.; Patil, C.; Saadi, M. A. S. R.; Xie, T.; Azadani, J. G.; Uluutku, B.; Amin, R.; Briggs, A. F.; Miscuglio, M.; Van Thourhout, D.; Solares, S. D.; Low, T.; Agarwal, R.; Bank, S. R.; Sorger, V. *Nat. Photonics* **2020,** 14, (9), 578-584.

(14) Androulidakis, C.; Koukaras, E. N.; Paterakis, G.; Trakakis, G.; Galiotis, C. *Nat. Commun.* **2020,** 11, (1), 1595.

(15) Jiang, J.; Chen, Z.; Hu, Y.; Xiang, Y.; Zhang, L.; Wang, Y.; Wang, G.-C.; Shi, J. *Nat. Nanotechnol.* **2021,** 16, (8), 894-901.

(16) Wang, S. W.; Medina, H.; Hong, K. B.; Wu, C. C.; Qu, Y.; Manikandan, A.; Su, T. Y.; Lee, P. T.; Huang, Z. Q.; Wang, Z.; Chuang, F. C.; Kuo, H. C.; Chueh, Y. L. *ACS Nano* **2017,** 11, (9), 8768-8776.

(17) Martella, C.; Ortolani, L.; Cianci, E.; Lamperti, A.; Morandi, V.; Molle, A. *Nano Res.* **2019,**

12, (8), 1851-1854.

(18) Liu, X.; Hu, S.; Luo, J.; Li, X.; Wu, J.; Chi, D.; Ang, K. W.; Yu, W.; Cai, Y. *Small* **2021,** 17, (43), e2100246.

(19) Li, H.; Contryman, A. W.; Qian, X.; Ardakani, S. M.; Gong, Y.; Wang, X.; Weisse, J. M.; Lee, C. H.; Zhao, J.; Ajayan, P. M.; Li, J.; Manoharan, H. C.; Zheng, X. *Nat. Commun.* **2015,** 6, 7381.

(20) Hong, J. Y.; Shin, Y. C.; Zubair, A.; Mao, Y.; Palacios, T.; Dresselhaus, M. S.; Kim, S. H.; Kong, J. *Adv. Mater.* **2016,** 28, (12), 2382-92.

(21) Wang, H.; Leong, W. S.; Hu, F.; Ju, L.; Su, C.; Guo, Y.; Li, J.; Li, M.; Hu, A.; Kong, J. *ACS Nano* **2018,** 12, (3), 2395-2402.

(22) Mangu, V. S.; Zamiri, M.; Brueck, S. R. J.; Cavallo, F. *Nanoscale* **2017,** 9, (43), 16602-16606.

(23) Lee, C.; Yan, H.; Brus, L. E.; Heinz, T. F.; Hone, J.; Ryu, S. *ACS nano* **2010,** 4, (5), 2695-2700.

(24) Li, H.; Zhang, Q.; Yap, C. C. R.; Tay, B. K.; Edwin, T. H. T.; Olivier, A.; Baillargeat, D. *Adv. Funct. Mater.* **2012,** 22, (7), 1385-1390.

(25) Desai, S. B.; Seol, G.; Kang, J. S.; Fang, H.; Battaglia, C.; Kapadia, R.; Ager, J. W.; Guo, J.; Javey, A. *Nano Lett.* **2014,** 14, (8), 4592-4597.

(26) Yang, L.; Cui, X.; Zhang, J.; Wang, K.; Shen, M.; Zeng, S.; Dayeh, S. A.; Feng, L.; Xiang, B. *Sci. Rep.* **2014,** 4, (1), 1-7.

(27) Lloyd, D.; Liu, X.; Christopher, J. W.; Cantley, L.; Wadehra, A.; Kim, B. L.; Goldberg, B. B.; Swan, A. K.; Bunch, J. S. *Nano Lett.* **2016,** 16, (9), 5836-41.

(28) Conley, H. J.; Wang, B.; Ziegler, J. I.; Haglund, R. F., Jr.; Pantelides, S. T.; Bolotin, K. I.

Nano Lett **2013,** 13, (8), 3626-30.

(29) Mak, K. F.; Lee, C.; Hone, J.; Shan, J.; Heinz, T. F. *Phys. Rev. Lett.* **2010,** 105, (13), 136805.

(30) Jeong, H. Y.; Kim, U. J.; Kim, H.; Han, G. H.; Lee, H.; Kim, M. S.; Jin, Y.; Ly, T. H.; Lee, S. Y.; Roh, Y. G.; Joo, W. J.; Hwang, S. W.; Park, Y.; Lee, Y. H. *ACS Nano* **2016,** 10, (9), 8192-8.

(31) Yang, Z.; Jie, W.; Mak, C. H.; Lin, S.; Lin, H.; Yang, X.; Yan, F.; Lau, S. P.; Hao, J. *ACS Nano* **2017,** 11, (4), 4225-4236.

(32) Kufer, D.; Konstantatos, G. *Nano Lett.* **2015,** 15, (11), 7307-13.

(33) Kim, K. S.; Ji, Y. J.; Kim, K. H.; Choi, S.; Kang, D. H.; Heo, K.; Cho, S.; Yim, S.; Lee, S.; Park, J. H.; Jung, Y. S.; Yeom, G. Y. *Nat. Commun.* **2019,** 10, (1), 4701.

(34) Boroditsky, M.; Vrijen, R.; Coccioli, R.; Bhat, R.; Yablonovitch, E. *J. Light. Technol.* **1999,** 17, (11), 2096.

(35) Shi, H.; Yan, R.; Bertolazzi, S.; Brivio, J.; Gao, B.; Kis, A.; Jena, D.; Xing, H. G.; Huang, L. *ACS nano* **2013,** 7, (2), 1072-1080.

(36) Zhang, H.; Zhang, X.; Liu, C.; Lee, S. T.; Jie, J. *ACS Nano* **2016,** 10, (5), 5113-22.

For Table of Contents Only